

# Electronic band structure of polytypical nanowhiskers: a theoretical approach based on group theory and k-p method

Faria Junior, P. E. and Sipahi, G. M.

*Instituto de Física de São Carlos, USP, São Carlos, SP, Brazil*

(Dated: February 14, 2012)

Semiconductor nanowhiskers made of III-V compounds exhibit great potential for technological applications. Controlling the growth conditions, such as temperature and diameter, it is possible to alternate between zinc blend and wurtzite crystalline phases, giving origin to the so called polytypism. This effect has great influence in the electronic and optical properties of the system, generating new forms of confinement to the carriers. A theoretical model capable to accurately describe electronic and optical properties in these polytypical nanostructures can be used to study and develop new kinds of nanodevices. In this study, we present the development of a wurtzite/zincblend polytypical model to calculate the electronic band structure of nanowhiskers based on group theory concepts and the k-p method. Although the interest is in polytypical superlattices, the proposed model was applied to a single quantum well of InP to extract the physics of the wurtzite/zincblend polytypism. By the analysis of our results, some trends can be predicted: spatial carriers' separation, predominance of perpendicular polarization (xy plane) in the luminescence spectra and interband transition blueshifts with strain. A possible range of values for the WZ InP spontaneous polarization was suggested.

## I. INTRODUCTION

Low dimensional semiconductor structures exhibit different characteristics, ruled by the size and morphology of the system. Recently, there is an increasing interest in nanowhiskers (NWs), also known as nanowires. These are one dimensional nanostructures grown perpendicular to the surface of the substrate, usually by the vapor-liquid-crystal (VLC) method. The technological applications of NWs, including biological and chemical nanosensors [1–3], lasers [4], light emission diodes [5] and field effect transistors [6], can be used in a large variety of fields.

The first register in the literature of whiskers was made by Wagner and Ellis [7] in 1964. In this classic study, it is demonstrated the vertical growth of a Si whisker in the [111] direction, activated by droplets of Au, using the VLC method. The radius of the structure is approximately the same as the catalyst droplet of Au and the vertical size depends on the ratio and time of the compound's deposition on the substrate. Although the VLC method is the most common, other methods like vapor-phase epitaxy (VPE), molecular-beam epitaxy (MBE) and magnetron deposition (MD) are also applied for the NWs growth.

In III-V compound NWs (e. g., arsenides and phosphides), a surprising characteristic is the predominance of the wurtzite (WZ) phase in the structure. Exception made for the nitrides, the stable crystalline structure of III-V compounds in the bulk form is zincblend (ZB). Although the difference between the small formation energy of the two phases are small, approximately of 20 meV per pair of atoms at zero pressure, high pressures would be necessary to obtain the WZ phase in the bulk form. However, reducing the dimensions of the system to the

nanoscale level, such as in these NWs, the WZ phase becomes more stable. This stability is due to the smaller surface energy of lateral faces compared to the cubic crystal. An extensive summary of NWs growth, properties and applications was made by Dubrovskii *et al.* [8].

Controlling the growth conditions, such as temperature and diameter of the NW, it is possible to create different regions composed of ZB and WZ structures [9–16]. The mixture of both crystalline phases in the same nanostructure is called polytypism. Such characteristic directly affects the electronic and optical properties of NWs. The detailed study of polytypism in III-V semiconductor NWs is fundamental to the development of novel functional nanodevices with a variety of features.

The theoretical tool to calculate the electronic band structure of polytypical NWs used in this paper is the k-p method. Although the formulation of this method has already been done for ZB and WZ crystal structures in the bulk form [17–21] and in superlattices and heterostructures [22–26], it was never applied to a polytypical case.

Deeply studying the core of the k-p formulation for both crystal structures and relying on the symmetry connection of the polytypical interface presented in the paper of Murayama e Nakayama [27], it was possible to describe the top valence bands and lower conduction bands of ZB and WZ in the same Hamiltonian matrix. The envelope function scheme was then applied to obtain the variation of the parameters along the growth direction, describing the different regions in a NW, thus completing the polytypical model. The effects of strain, spontaneous polarization and piezoelectric polarization are also included in the model.

In order to test the model, it was applied to a polytypical WZ/ZB/WZ quantum well of InP. Although a real

NW is composed by several regions of WZ and ZB, the physical trends of the polytypical interface can be extracted from a single quantum well system. We choose the InP compound basically for two reasons: the small spin-orbit energy makes easier to fit the matrix parameters to the effective mass values given in the paper of De and Pryor [28] for the WZ polytype and also because the InP NWs can be found in a great number of studies in the present literature [9, 29–35].

The present paper is divided as follows: In section II we discuss the symmetry of ZB and WZ crystal structures and analyze how the irreducible representations of the energy bands are connected in the polytypical interface. Section III describes the Hamiltonian terms for the polytypical model. The results, and their discussion, of InP WZ/ZB/WZ single well are found in section IV. Finally, in section V, we draw our conclusions.

## II. SYMMETRY ANALYSIS

### A. Zincblend and wurtzite structures

Our formulation relies on group theory concepts and therefore it is necessary to understand the symmetry of the two crystal structures considered in the polytypical NWs. The ZB structure belongs to the class of symmorphic space groups and has the  $T_d$  symmetry as its factor group. The number of atoms in the primitive unit cell is two. Unlike ZB, the WZ structure belongs to the class of nonsymmorphic space groups and its factor group is isomorphic to  $C_{6v}$ . The classes of symmetry operations  $C_2$ ,  $C_6$  and  $\sigma_v$  are followed by a translation of  $c/2$  in the  $[0001]$  direction. WZ has four atoms in the primitive unit cell. Comparing the factor groups one can notice that  $C_{6v}$  is less symmetric than  $T_d$ . In the k-p framework, this lower symmetry decreases the number of irreducible representations (IRs) in the group consequently increasing the number of interactions in the Hamiltonian. A good description of the concepts of space group symmetry can be found in Ref. [36].

In polytypical NWs, the common growth direction is the ZB  $[111]$ , which exhibit a noticeable similarity to WZ  $[0001]$ . Actually, analyzing both crystal structures in these directions, one can describe them as stacked hexagonal layers. The ZB has three layers in the stacking sequence (ABCABC) while WZ has only two (ABAB) as shown in Figure 1. The crystal structure alternation occurs when a stacking fault happens in WZ, leading to a single ZB segment, or when two twin planes appear in ZB, originating a single WZ segment [11].

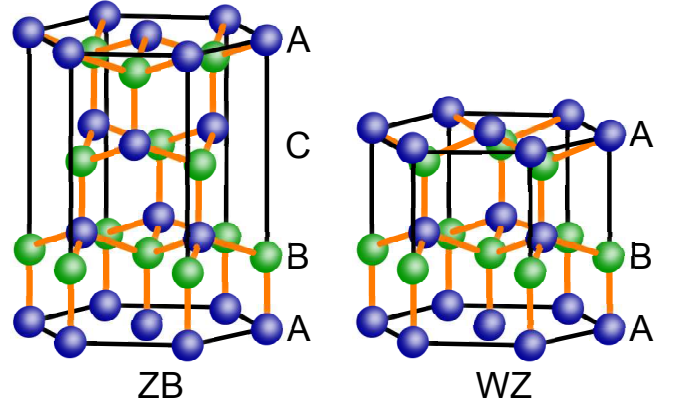


Figure 1. ZB (left) and WZ (right) structures and their stacking sequence. The ZB is presented in the  $[111]$  direction. In this direction, the unit cell is twice as large as the usual ZB unit cell [27].

### B. Irreducible representations at the polytypical interface

An important issue of the model is how to connect the energy levels at the polytypical interface depending on the symmetry they assume. Based on the scheme presented by Murayama and Nakayama [27] of single group IRs at the WZ/ZB interface the symmetry of the energy bands can be chosen. The same scheme was constructed by De and Pryor [28] for the double group IRs with the inclusion of the spin-orbit coupling.

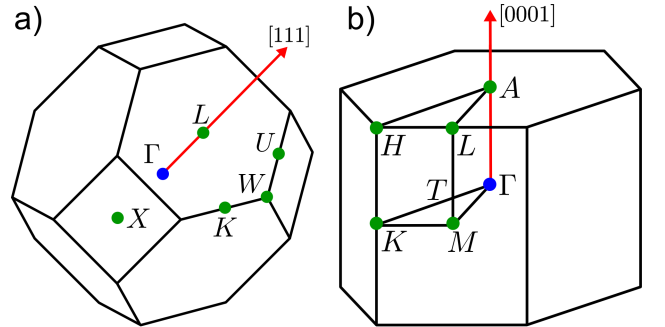


Figure 2. Usual a) ZB and (b) WZ first Brillouin zones and their respective high symmetry points. The arrows (red line) represent the growth directions in NWs. For ZB, the  $[111]$  direction is directed towards the L-point.

Since WZ has twice more atoms in the primitive unit cell than ZB, the number of energy bands in the  $\Gamma$ -point is also twice as large. Considering the  $sp^3$  hybridization, without spin, ZB has 8 energy bands while WZ has 16. However, in the  $[111]$  direction, the ZB unit cell is two times larger than the usual face-centered cubic (FCC) unit cell [27]. In the IRs scheme mentioned above, the presence of energy bands with  $L$  symmetry takes into account the mismatch in the number of atoms for the

usual unit cells. The reason for the appearance of the  $L$  symmetry is the fact that ZB [111] growth direction is directed towards the  $L$ -point, as displayed in Figure 2a, hence this point is mapped out in the  $\Gamma$ -point. Figure 2b, displays the first Brillouin zone (FBZ) for the WZ structure.

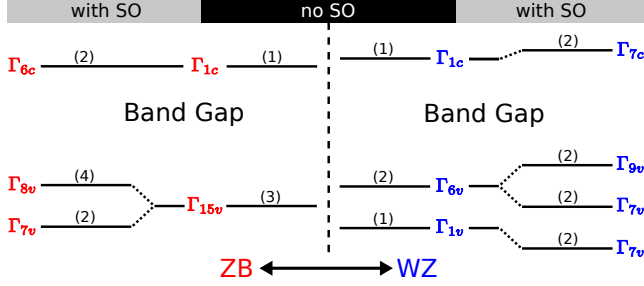


Figure 3. The subset of IRs considered in this formulation with and without the spin-orbit (SO) coupling. The numbers in parentheses are the degeneracy of the IRs. The notation for the IRs follow Refs. [27, 28]

Among all the IRs presented in Refs. [27, 28] we considered only a small subset. Displayed in Figure 3, this subset comprises the lower conduction band and the top three valence bands, which belong to the  $\Gamma$ -point in both structures. The price that is paid in considering only a small subset is the accuracy of the Hamiltonian for a fraction of the FBZ, approximately 10-20%. The basis states for the IRs of the considered bands are presented in equations (1) and (2) for ZB and WZ, respectively.

$$\begin{aligned}\Gamma_{1c}^{ZB} &\sim x^2 + y^2 + z^2 \\ \Gamma_{15v}^{ZB} &\sim (x, y, z)\end{aligned}\quad (1)$$

$$\begin{aligned}\Gamma_{1c}^{WZ} &\sim x^2 + y^2 + z^2 \\ \Gamma_{6v}^{WZ} &\sim (x, y) \\ \Gamma_{1v}^{WZ} &\sim z\end{aligned}\quad (2)$$

Although the IRs belong to different symmetry groups ( $T_d$  and  $C_{6v}$ ), the basis states transform as the usual  $x, y, z$  cartesian coordinates for the valence bands and the scalar  $x^2 + y^2 + z^2$  for the conduction band in both crystal structures. This information is crucial to represent WZ and ZB with the same Hamiltonian and is the essential insight of our formulation.

### III. THEORETICAL MODEL

#### A. k·p Hamiltonian

In order to develop our k·p Hamiltonian [37] it is convenient to describe the ZB structure in a coordinate system that has the  $z$  axis parallel to the growth direction. This coordinate system is the primed one presented in Figure 4. Even though the choice of the coordinate system is arbitrary, it alters the k·p Hamiltonian. For example, in the unprimed coordinate system the  $k_z$  direction is directed towards the  $X$ -point but in the primed coordinate system it is directed towards the  $L$ -point. Thus our expectation is that an anisotropy in the ZB Hamiltonian between the  $k_x$  and  $k_z$  directions will occur since they are not reaching equivalent points in the the reciprocal space anymore.

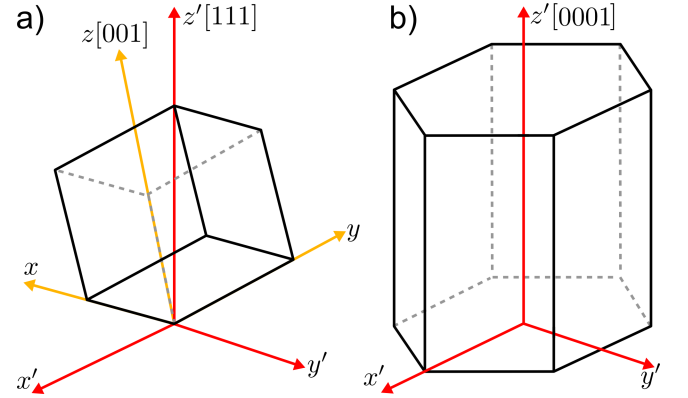


Figure 4. (a) ZB conventional unit cell with two different coordinate systems. (b) WZ conventional unit cell with its common coordinate system. The [111] growth direction for ZB structure passes along the main diagonal of the cube and is represented in the primed coordinate system.

Considering the single group formulation of the k·p method, the choice of the coordinate system defines the symmetry operation matrices used to derive the momentum matrix elements. It is necessary to recalculate the Hamiltonian terms for the ZB structure. However, the energy bands we consider here are exactly the ones customary used in the ZB [001] k·p Hamiltonian. Instead of recalculating the terms for ZB [111] k·p Hamiltonian it is possible, and also useful, to apply a basis rotation to the ZB [001] matrix. This rotation procedure is well described in the paper of Park and Chuang [38].

The basis set for both crystal structures in the primed coordinate system (the prime will be dropped out of the notation from now on and will be used only when it is necessary) is given by

$$\begin{aligned}
|c_1\rangle &= -\frac{1}{\sqrt{2}} |(X + iY) \uparrow\rangle \\
|c_2\rangle &= \frac{1}{\sqrt{2}} |(X - iY) \uparrow\rangle \\
|c_3\rangle &= |Z \uparrow\rangle \\
|c_4\rangle &= \frac{1}{\sqrt{2}} |(X - iY) \downarrow\rangle \\
|c_5\rangle &= -\frac{1}{\sqrt{2}} |(X + iY) \downarrow\rangle \\
|c_6\rangle &= |Z \downarrow\rangle \\
|c_7\rangle &= i |S \uparrow\rangle \\
|c_8\rangle &= i |S \downarrow\rangle
\end{aligned} \tag{3}$$

In a first approximation, the interband interaction is not taken into account explicitly here, thus the conduction band is a single band model for spin-up and spin-down reading as

$$E_C(\vec{k}) = E_g + E_0 + \frac{\hbar^2}{2m_e^\parallel} k_z^2 + \frac{\hbar^2}{2m_e^\perp} (k_x^2 + k_y^2) \tag{4}$$

where  $E_g$  is the band gap,  $E_0$  is the energy reference at  $\vec{k} = 0$  and  $m_e^\parallel$ ,  $m_e^\perp$  are the electron effective masses parallel and perpendicular do the  $z$  axis, respectively. For the ZB structure, however, the electron effective masses are equal.

The Hamiltonian for WZ and ZB valence band is given by

$$H_V(\vec{k}) = \begin{bmatrix} F & -K^* & -H^* & 0 & 0 & 0 \\ -K & G & H & 0 & 0 & \Delta \\ -H & H^* & \lambda & 0 & \Delta & 0 \\ 0 & 0 & 0 & F & -K & H \\ 0 & 0 & \Delta & -K^* & G & -H^* \\ 0 & \Delta & 0 & H^* & -H & \lambda \end{bmatrix} \tag{5}$$

and the matrix terms are defined as

$$\begin{aligned}
F &= \Delta_1 + \Delta_2 + \lambda + \theta \\
G &= \Delta_1 - \Delta_2 + \lambda + \theta \\
\lambda &= A_1 k_z^2 + A_2 (k_x^2 + k_y^2) \\
\theta &= A_3 k_z^2 + A_4 (k_x^2 + k_y^2) \\
K &= A_5 k_+^2 + 2\sqrt{2} A_z k_- k_z \\
H &= A_6 k_+ k_z + A_z k_-^2 \\
\Delta &= \sqrt{2} \Delta_3
\end{aligned} \tag{6}$$

where  $k_\alpha$  ( $\alpha = x, y, z$ ) are the wave vectors in the primed

coordinate system,  $A_i$  ( $i = 1, \dots, 6, z$ ) are the holes effective mass parameters,  $\Delta_1$  is the crystal field splitting energy in WZ,  $\Delta_{2,3}$  are the spin-orbit coupling splitting energies and  $k_\pm = k_x \pm i k_y$ .

It is important to notice that the parameter  $A_z$  appears in the matrix elements to regain the original isotropic symmetry of the ZB band structure in the new coordinate system. In the regions of WZ crystal structure, this parameter is zero and the matrix is exactly the canonical in use for WZ crystals.

Although this is not the usual way to describe ZB crystals, all the parameters in the matrix can be related to the familiar  $\gamma_i$  ( $i = 1, 2, 3$ ) and  $\Delta_{SO}$  as shown above

$$\begin{aligned}
\Delta_1 &= 0 \\
\Delta_2 &= \Delta_3 = \frac{\Delta_{SO}}{3} \\
A_1 &= -\gamma_1 - 4\gamma_3 \\
A_2 &= -\gamma_1 + 2\gamma_3 \\
A_3 &= 6\gamma_3 \\
A_4 &= -3\gamma_3 \\
A_5 &= -\gamma_2 - 2\gamma_3 \\
A_6 &= -\sqrt{2} (2\gamma_2 + \gamma_3) \\
A_z &= \gamma_2 - \gamma_3
\end{aligned} \tag{7}$$

One may also argue that this formulation is very similar to the WZ phase. The insight here is to consider ZB as a WZ structure without the crystal field splitting energy. Since the WZ structure is less symmetric than ZB, as mentioned in section II.A, it is possible to represent the ZB parameters with the WZ ones.

The resulting valence band structures for bulk WZ and ZB InP using matrix (5) are shown in Figure 5. The presence of the crystal field in the WZ structure creates three distinct two-fold degenerate bands whereas in ZB there is a four-fold and a two-fold degenerate set of bands. Additionally, the anisotropy between  $k_x$  and  $k_y$  is evident in both crystal structures. In WZ it is due to the different symmetry properties of the  $xy$ -plane and the  $z$  axis but in ZB it is because  $k_x$  and  $k_z$  directions do not reach equivalent points in the reciprocal space. Since the conduction band is a parabolic model, we did not present its dispersion relation. The ZB parameters were obtained from Ref. [39] and the WZ parameters were derived using the effective masses presented in Ref. [28]. These parameters can be found in Table I.

Following Chuang and Chang [40] notation, the valence energy bands for WZ are named after the composition of the states at  $\vec{k} = 0$ . HH (heavy hole) states are composed only by  $|c_1\rangle$  or  $|c_4\rangle$ , LH (light hole) states are composed mainly of  $|c_2\rangle$  or  $|c_5\rangle$  and CH (crystal-field split-off hole) are composed mainly of  $|c_3\rangle$  or  $|c_6\rangle$ . For the ZB structure the common identification of the valence energy bands

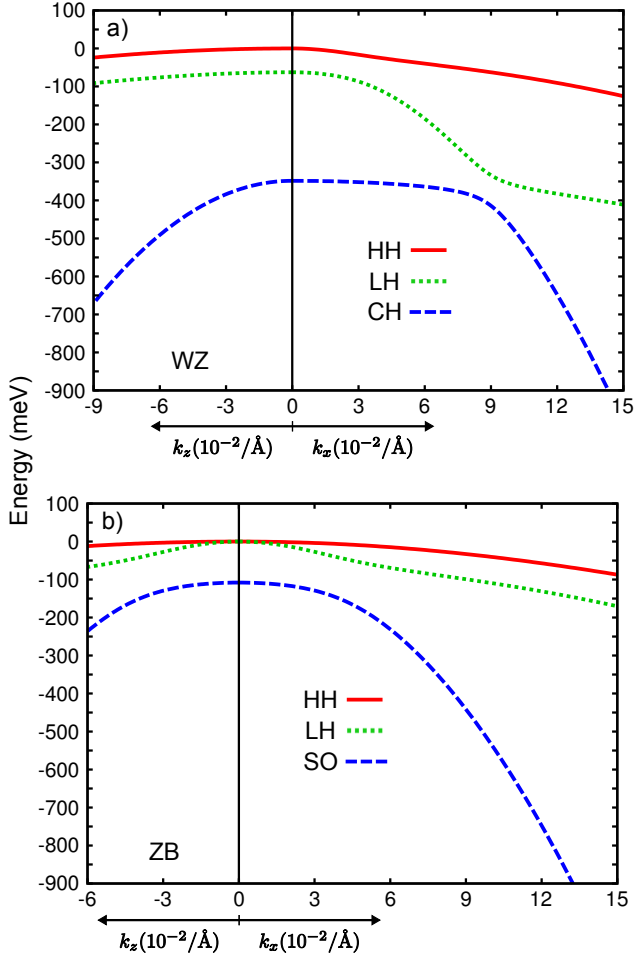


Figure 5. Valence band structure for bulk (a) WZ and (b) ZB in the primed coordinate system. The usual identification of the bands was used for ZB while in WZ it was necessary to analyze the composition of the states in the  $\Gamma$ -point. We can see the anisotropy between  $k_z$  and  $k_x$  in WZ and also in ZB because in the new coordinate system the  $x$  and  $z$  axes do not reach equivalent points in the reciprocal space. The top of the valence band in both crystal structures was chosen to be at zero.

was used. The four-fold degenerate bands at  $\vec{k} = 0$  are HH and LH and the lower two-fold degenerate band is SO (split-off hole).

### B. Strain

The strain Hamiltonian can be obtained using the same basis rotation applied to the k-p matrix [38]. Similarly, the conduction and valence band are decoupled.

For the conduction band, the strain effect is given by

$$E_{C\varepsilon} = a_{c\parallel}\varepsilon_{zz} + a_{c\perp}(\varepsilon_{xx} + \varepsilon_{yy}) \quad (8)$$

Table I. InP parameters used in the calculations.

Parameter	ZB InP	WZ InP
Lattice constant ( $\text{\AA}$ )		
$a$	5.8697	4.1505
$c$	-	6.7777
Energy parameters (eV)		
$E_g$	1.4236	1.474
$\Delta_1$	0	0.303
$\Delta_2 = \Delta_3$	0.036	0.036
Conduction band effective masses		
$m_e^{\parallel}/m_0$	0.0795	0.105
$m_e^{\perp}/m_0$	0.0795	0.088
Valence band effective mass parameters (units of $\frac{\hbar^2}{2m_0}$ )		
$A_1$	-13.4800	-10.7156
$A_2$	-0.8800	-0.8299
$A_3$	12.6000	9.9301
$A_4$	-6.3000	-5.2933
$A_5$	-5.8000	5.0000
$A_6$	-7.4953	1.5000
$A_z$	-0.5000	0

where  $a_{c\parallel}$  and  $a_{c\perp}$  are the conduction band deformation potentials parallel and perpendicular to the  $z$  axis, respectively. In the ZB structure they have the same value.

The valence band strain Hamiltonian is

$$H_{V\varepsilon} = \begin{bmatrix} F_{\varepsilon} & -K_{\varepsilon}^* & -H_{\varepsilon}^* & 0 & 0 & 0 \\ -K_{\varepsilon} & F_{\varepsilon} & H_{\varepsilon} & 0 & 0 & 0 \\ -H_{\varepsilon} & H_{\varepsilon}^* & \lambda_{\varepsilon} & 0 & 0 & 0 \\ 0 & 0 & 0 & F_{\varepsilon} & -K_{\varepsilon} & H_{\varepsilon} \\ 0 & 0 & 0 & -K_{\varepsilon}^* & F_{\varepsilon} & -H_{\varepsilon}^* \\ 0 & 0 & 0 & H_{\varepsilon}^* & -H_{\varepsilon} & \lambda_{\varepsilon} \end{bmatrix} \quad (9)$$

and the matrix terms are

$$\begin{aligned} F_{\varepsilon} &= (D_1 + D_3)\varepsilon_{zz} + (D_2 + D_4)(\varepsilon_{xx} + \varepsilon_{yy}) \\ \lambda_{\varepsilon} &= D_1\varepsilon_{zz} + D_2(\varepsilon_{xx} + \varepsilon_{yy}) \\ K_{\varepsilon} &= D_5^{(1)}(\varepsilon_{xx} - \varepsilon_{yy}) + D_5^{(2)}2i\varepsilon_{xy} \\ H_{\varepsilon} &= D_6(\varepsilon_{xz} + i\varepsilon_{yz}) + D_z(\varepsilon_{xx} - \varepsilon_{yy}) \end{aligned} \quad (10)$$

where  $D_i$ 's are the valence band deformation potentials and  $\varepsilon_{ij}$  is the strain tensor.

In the same way as the  $A_z$  parameter appears in k-p

matrix, some extra deformation potential terms were appears to use the same strain Hamiltonian for both crystal structures. The deformation potential  $D_5$  was split in two parts because the strain tensor  $\varepsilon_{xy}$  is not present in the ZB structure. For WZ,  $D_5^{(1)} = D_5^{(2)}$ . Also, the  $D_z$  deformation potential takes into account the non existing term  $\varepsilon_{xx} - \varepsilon_{yy}$  in the WZ structure.

The deformation potentials  $D_i$ 's are related to the ZB ones

$$\begin{aligned}
D_1 &= a_v + \frac{2d}{\sqrt{3}} \\
D_2 &= a_v - \frac{d}{\sqrt{3}} \\
D_3 &= -\sqrt{3}d \\
D_4 &= \frac{3d}{2\sqrt{3}} \\
D_5^{(1)} &= -\frac{b}{2} - \frac{d}{\sqrt{3}} \\
D_5^{(2)} &= 0 \\
D_6 &= 0 \\
D_z &= -\frac{b}{2} + \frac{d}{2\sqrt{3}} \\
a_{c\parallel} &= a_{c\perp} = a_c
\end{aligned} \tag{11}$$

Considering biaxial strain, the elements of the strain tensor can be obtained in both coordinate systems for ZB and WZ. Although it is convenient to describe the Hamiltonian terms in the primed coordinate system, it is also useful to describe the strain tensor elements in the unprimed coordinate system. They will be used to construct the piezoelectric polarization in section III.C. The prime will be reintegrated in the notation to avoid confusion and the upper scripts  $z$  and  $w$  denotes the ZB and WZ structures, respectively.

For the primed coordinate system, the elements of the strain tensor are given by

$$\varepsilon_{xx}'^{(z,w)} = \varepsilon_{yy}'^{(z,w)} = \frac{a_0 - a^{(z,w)}}{a^{(z,w)}} \tag{12}$$

$$\varepsilon_{zz}'^{(z)} = -\frac{1}{\sigma^{(111)}} \varepsilon_{xx}'^{(z)} \tag{13}$$

$$\varepsilon_{zz}'^{(w)} = -\frac{2C_{13}^{(w)}}{C_{33}^{(w)}} \varepsilon_{xx}'^{(w)} \tag{14}$$

$$\varepsilon_{yz}'^{(z,w)} = \varepsilon_{zx}'^{(z,w)} = \varepsilon_{xy}'^{(z,w)} = 0 \tag{15}$$

where  $a_0$  is the lattice constant of the substrate.

In the unprimed coordinate system, the strain tensor elements assume the form

$$\varepsilon_{xx}^{(z)} = \varepsilon_{yy}^{(z)} = \varepsilon_{zz}^{(z)} = \frac{1}{3} \left( 2 - \frac{1}{\sigma^{(111)}} \right) \varepsilon_{xx}'^{(z)} \tag{16}$$

$$\varepsilon_{yz}^{(z)} = \varepsilon_{zx}^{(z)} = \varepsilon_{xy}^{(z)} = -\frac{1}{3} \left( 1 + \frac{1}{\sigma^{(111)}} \right) \varepsilon_{xx}'^{(z)} \tag{17}$$

The quantity  $\sigma^{(111)}$  is given by

$$\sigma^{(111)} = \frac{C_{11}^{(z)} + 2C_{12}^{(z)} + 4C_{44}^{(z)}}{2C_{11}^{(z)} + 4C_{12}^{(z)} - 4C_{44}^{(z)}} \tag{18}$$

Comparing the expression (13) with (14) it is possible to obtain effective values for  $C_{13}^{(z)}$  and  $C_{33}^{(z)}$  for ZB in the primed coordinate system. The effective values are:

$$C_{13}^{(z)} = C_{11}^{(z)} + 2C_{12}^{(z)} - 2C_{44}^{(z)} \tag{19}$$

$$C_{33}^{(z)} = C_{11}^{(z)} + 2C_{12}^{(z)} + 4C_{44}^{(z)} \tag{20}$$

Thus, we have a single set of expressions to describe biaxial strain in the primed coordinate system for ZB and WZ crystal structures:

$$\varepsilon_{xx}' = \varepsilon_{yy}' = \frac{a_0 - a}{a} \tag{21}$$

$$\varepsilon_{zz}' = -\frac{2C_{13}^{(z,w)}}{C_{33}^{(z,w)}} \varepsilon_{xx}' \tag{22}$$

$$\varepsilon_{yz}' = \varepsilon_{zx}' = \varepsilon_{xy}' = 0 \tag{23}$$

Since deformation potentials and elastic stiffness constants for WZ InP are not yet available in the literature, we will consider here that the strain effect appears only in the ZB structure. This assumption is not totally unrealistic because WZ is the dominant phase in the NW.

Figure 6 shows the effect of strain at  $\vec{k} = 0$  for the diagonalized Hamiltonian ( $\mathbf{k} \cdot \mathbf{p}$  and strain terms) as a function of the percentage of strain tensor. A linear variation for the conduction band and the HH band is observed, however, the LH and SO bands have a non-linear behavior. The order of the HH and LH bands changes when strain is distensive. Table II lists the ZB parameters used in

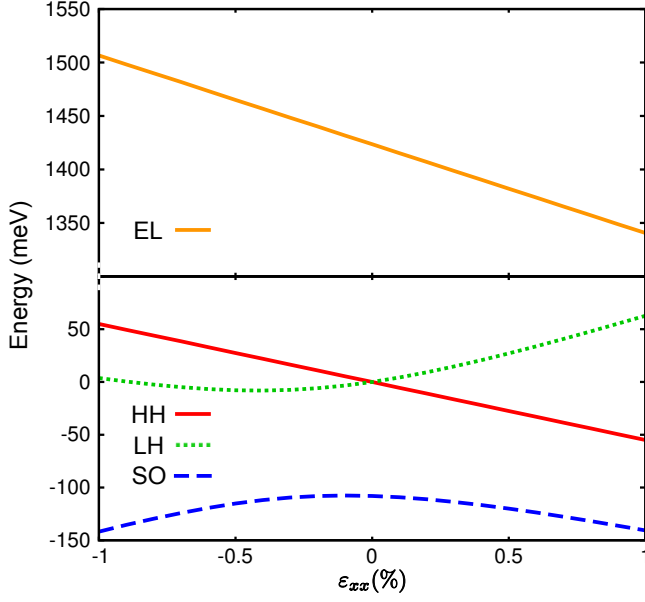


Figure 6. Strain effect in the band edges of ZB InP as a function of the percentage of strain tensor. EL and HH shows a linear variation while LH and SO shows a nonlinear behavior. The strain effect removes the HH and LH degeneracy.

the calculations.

Table II. ZB InP strain parameters.

Parameter	ZB InP
Deformation potentials (eV)	
$D_1$	-6.3735
$D_2$	2.2868
$D_3$	8.6603
$D_4$	-4.3301
$D_5^{(1)}$	3.8868
$D_5^{(2)}$	0
$D_6$	0
$D_z$	-0.4434
$a_c$	-6.0
$a_{c\perp}$	-6.0
Elastic stiffness constant (GPa)	
$C_{11}$	1011
$C_{12}$	561
$C_{44}$	456

### C. Spontaneous and Piezoelectric Polarization

Piezoelectric polarization appears when a crystal is subjected to strain. In ZB semiconductors grown along the [111] direction, the magnitude of the piezoelectric polarization, in the unprimed coordinate system of Fig. 4, is given by [41]:

$$P_i = 2e_{14}\varepsilon_{jk} \quad (24)$$

where  $e_{14}$  is the piezoelectric constant for ZB materials,  $(i, j, k)$  are the cartesian coordinates  $(x, y, z)$  in a cyclic order and  $\varepsilon_{jk}$  are the strain tensor components.

Applying the coordinate system rotation in the piezoelectric polarization vector components in order to describe them in the primed coordinate system we obtain:

$$\begin{aligned} P'_x &= \frac{1}{\sqrt{6}} (P_x + P_y - 2P_z) = 0 \\ P'_y &= \frac{1}{\sqrt{2}} (-P_x + P_y) = 0 \\ P'_z &= \frac{1}{\sqrt{3}} (P_x + P_y + P_z) = \sqrt{3}P \end{aligned} \quad (25)$$

The resulting piezoelectric polarization alongside the growth direction is then:

$$P'_z = -\frac{2}{\sqrt{3}}e_{14} \left( 1 + \frac{1}{\sigma_{(111)}} \right) \varepsilon'_{xx} \quad (26)$$

The spontaneous polarization effect in WZ structure is due to the relative displacement between the cations and anions when the ratio  $c/a$  is different from the ideal value in the WZ structure.

In a heterostructure, the effect of the different polarizations in each region creates an electric field through the whole structure. The net electric field in a determined layer,  $i$ , due to spontaneous and piezoelectric polarizations in the system is given by [42]:

$$E_i = \frac{\sum_{j=1}^N (P_j - P_i) \frac{l_j}{\varepsilon_j}}{\varepsilon_i \sum_{j=1}^N \frac{l_j}{\varepsilon_j}} \quad (27)$$

where  $j$  sums all over the layers in the heterostructure with polarization  $P$ , dielectric constant  $\varepsilon$  and length  $l$ .



### D. Effective mass equation in reciprocal space

The envelope function approximation [22, 43] is applied to couple the different crystal structures alongside the growth direction in the NW. In each region the wave function is expanded in terms of the Bloch functions of the corresponding polytype. Thus, the wave function of the whole system is given by:

$$\psi(\vec{r}) = \sum_l e^{i(\vec{k} \cdot \vec{r})} g_l(\vec{r}) u_l^{(WZ, ZB)}(\vec{r}) \quad (28)$$

where  $g_l(\vec{r})$  are the envelope functions of the  $l$ -th basis state.

Considering different Bloch functions for each region, the Hamiltonian parameters vary alongside the growth direction, making it possible to use the common k-p and strain matrices, (5) and (9), for both crystal structures. Moreover, since each crystal structure dictates its symmetry to their respective Bloch functions, some matrix elements can be forbidden by symmetry in the region of a certain crystalline phase. For example, the  $A_z$  parameter is zero in WZ regions whereas the  $\Delta_1$  parameter is zero in ZB regions.

To represent the growth dependence of the Hamiltonian parameters and envelope functions, the plane wave expansion is used. This formalism considers the periodicity of the whole system allowing the expansion of growth dependent functions in Fourier coefficients:

$$U(\vec{r}) = \sum_{\vec{K}} U_{\vec{K}} e^{i\vec{K} \cdot \vec{r}} \quad (29)$$

where  $U_{\vec{K}}$  are the Fourier coefficients of the function  $U(\vec{r})$  and  $\vec{K}$  is a reciprocal lattice vector. The Fourier expansion also induces the change  $\vec{k} \rightarrow \vec{k} + \vec{K}$  in the k-p matrix.

## IV. RESULTS AND DISCUSSION

The NW system chosen to apply our model is a WZ/ZB/WZ single well structure. Although a real NW is composed of multiple polytypical quantum wells with different sizes, the analysis of just a single well can bring out the physics of the polytypical interface. The effects of lateral confinement are neglected in a first approach, assuming NWs with large lateral dimensions. Strain, piezoelectric and spontaneous polarization are also included in the single well system.

When both crystal structures are put side by side, a band-offset is created at the interface, originating a confinement profile. The band mismatch is also taken from reference [28]. Figure 7 exhibits the WZ/ZB interface

for InP in two different schemes: in the left, the energies in  $\vec{k} = 0$  for the diagonalized Hamiltonian and in the right, the diagonal terms of the Hamiltonian. Although the composition of the states in the diagonalized energy bands are the same in  $\vec{k} = 0$ , the matrix is not constructed in this basis. Since the variation along the growth direction of the matrix elements is well defined, the scheme in the right is more convenient to analyze the potential profile of the system.

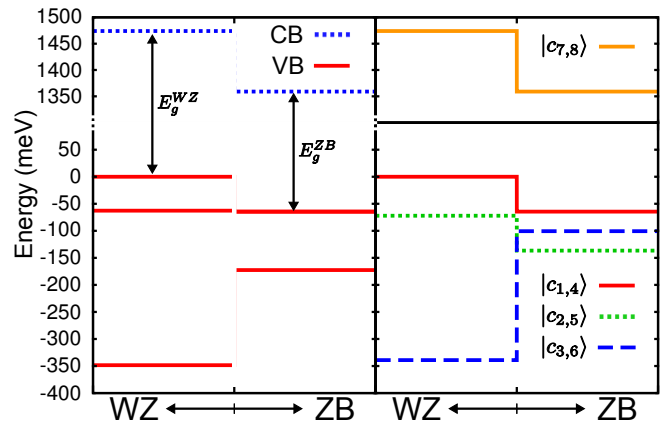


Figure 7. Left side: Band edge energies at  $\vec{k} = 0$  for the diagonalized Hamiltonian. Right side: Diagonal terms of the Hamiltonian at  $\vec{k} = 0$ .

In all performed calculations, the entire length of the system is set to 500 Å and the width of the ZB region,  $l$ , is variable. Figure 8 shows the single well potentials with and without the effect of strain. Since the potential profiles exhibits a type-II behavior, we expect a spatial separation of the carriers: electrons are more likely to be in the ZB region and the holes in the WZ region.

The strain considered here,  $-0.8\%$ , is an intermediate value between two data available in the literature from *ab initio* calculations. Reference [34] shows that the deviation between the lattice constant of ZB[111] and WZ[0001] is  $-1.3\%$  and reference [33] shows  $-0.3\%$ . Also, reference [32] suggests a difference slighter than  $0.5\%$  between the lattice constants of the two polytypes. The effect of strain shallows the potential wells in the conduction and valence bands, reducing the confinement of the carriers. We expect to have less confined states for the strained potential compared to the unstrained one.

The conduction and valence band structures for the potential profile without strain are presented in Fig. 9 for three different widths of the ZB region. The calculations were performed up to 10% in the  $\Gamma - T$  direction and 100% in the  $\Gamma - A$  direction. For the valence band 64 energy states are presented while only 18 are presented for the conduction band. Since the system has no asymmetric potential, the energy bands are two-fold degenerate in spin, therefore 32 states are visible in the valence



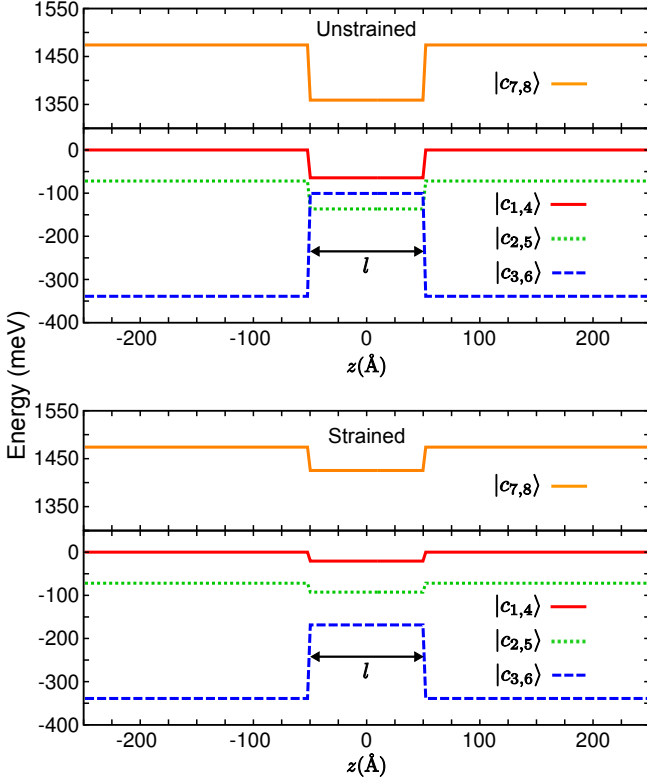


Figure 8. Diagonal potential profile of the Hamiltonian for the polytypical InP system with and without strain. The width of the ZB region,  $l$ , can change but the whole system's dimension remains constant with 500 Å.

band and 9 in the conduction band. For the three different values of  $l$ , the conduction energy bands are nominated, from bottom to top, as EL1-EL9, composed of  $|c_{7,8}\rangle$  states. The valence bands, from top to bottom, are nominated as HH1-19, LH1-4, HH20-21, LH5-7, HH22-23, LH8-9 for  $l = 100$  Å; HH1-16, LH1-2, HH17, LH3, HH18, LH4, HH19, LH5-7, HH20-21, LH8-9, HH22-23 for  $l = 160$  Å and HH1-14, LH1-2, HH15, LH3, HH16-17, LH4-5, HH18, LH6, HH19, LH7, HH20, LH8, HH21, LH9, HH22, LH10 for  $l = 200$  Å.

Since the highest valence band states are HH there is no significant anticrossing among the energy bands in the  $\Gamma - T$  direction. The anticrossing is characteristic of interactions between HH and LH bands in ZB and WZ quantum well structures. A slight anticrossing, however, can be seen in the energy region just above  $-75$  meV, which is next to the interaction region of the  $|c_{1,4}\rangle$  and  $|c_{2,5}\rangle$  profiles.

Increasing the value of  $l$  we find that the number of confined states in the conduction band increases. On the other hand, for the valence band the number of confined states decreases because the WZ region's width also decreases.

For the strained potential profile, the band structures

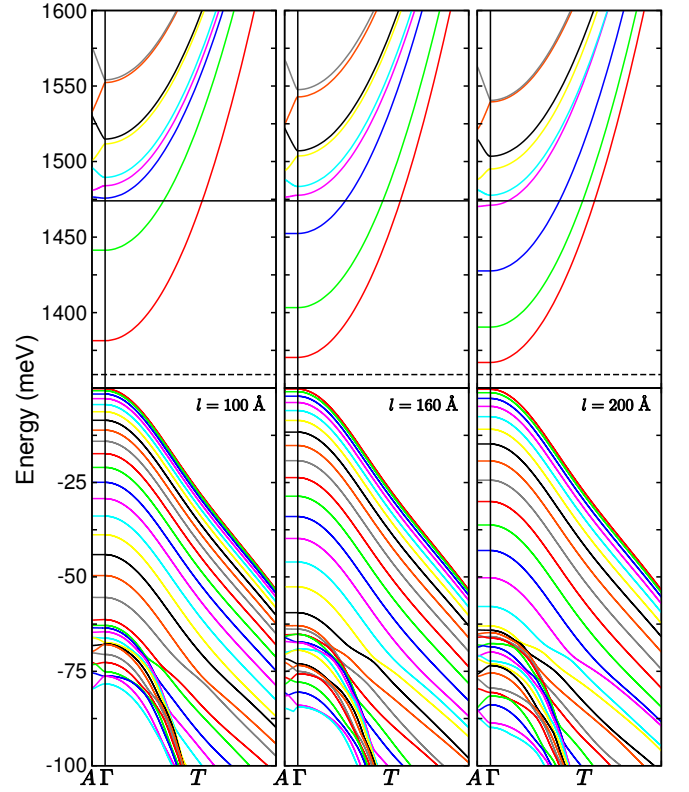


Figure 9. Band structure for the unstrained profile in Figure 8. The solid horizontal line is the top energy of conduction band well and the dashed horizontal line is the bottom energy of the conduction band well. The  $\Gamma - T$  direction refers to  $k_x$  and  $\Gamma - A$  to  $k_z$ .

for three different widths of the ZB region are displayed in Figure 10. The calculations were performed considering the same extension for the FBZ of the unstrained band structure. For the three different values of  $l$ , the conduction energy bands are nominated, from bottom to top, as EL1-EL9, composed of  $|c_{7,8}\rangle$  states. The valence bands, from top to bottom, are nominated as HH1-22, LH1, HH23, LH2-7, HH24-25 for  $l = 100$  Å; HH1-21, LH1-3, HH22-23, LH4-8, HH24 for  $l = 160$  Å and HH1-21, LH1-4, HH22-23, LH5-9 for  $l = 200$  Å.

As expected, the number of confined states for the strained profile compared to the unstrained one is smaller. Nonetheless, the similar confinement trend is visible here when the value of  $l$  increases: the number of confined states in the conduction band increases while in valence band decreases.

An interesting feature presented in the strained band structure is the presence of some confined states below the top region, around  $-62$  meV. This suggests a confinement in the intermediate region of the  $|c_{2,5}\rangle$  and  $|c_{3,6}\rangle$  profiles. Note that the coupling of these two profiles at  $\vec{k} = 0$  happens because of the off-diagonal spin-orbit term.

The composition of the energy states at  $\vec{k} = 0$  in the band structure is similar for the strained and unstrained cases: they are just HH or LH states. There is no CH states in the energy range considered here. The major contribution for CH states comes from the  $|c_{3,6}\rangle$  profile, which is the lowest one in both cases.

The information of the energy states' composition can reveal important trends in the luminescence spectra for this kind of system. For example, at  $\vec{k} = 0$  the dominant symmetry of the energy states belongs to  $(x, y)$ , which means that the luminescence spectra is more intense perpendicular to the growth direction. However, experimental measurements [31] indicates that the intensities perpendicular and parallel to the growth direction are almost similar. Therefore, we expect that the contribution for the parallel luminescence comes from the states at  $\vec{k} \neq 0$ . For  $\vec{k}$  points away from the  $\Gamma$ -point, there is a stronger mixing between all the basis states.

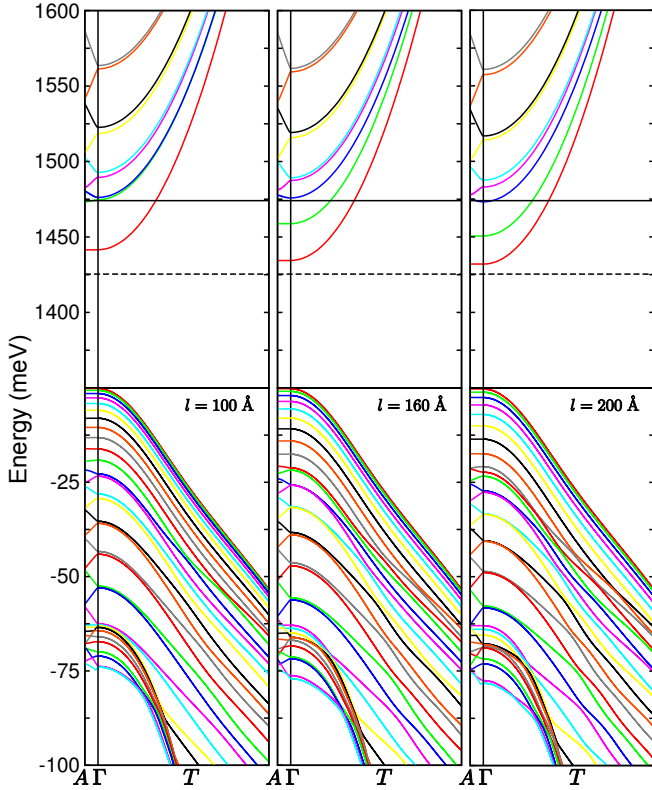


Figure 10. Band structure for the strained profile in Fig. 8. The solid and dashed lines have the same meaning as in Figure 9. The  $\Gamma - T$  direction refers to  $k_x$  and  $\Gamma - A$  to  $k_z$ .

The effect of the ZB region width for both strained and unstrained potential profile for the conduction and valence band states at  $\vec{k} = 0$  is presented in Figure 11. It is possible to observe that the number of confined states in the conduction band increases as the value of  $l$  increases. On the other hand, the number of confined states in the valence band decreases. Nevertheless,

the effect of the variation of  $l$  is more significant for the conduction band since the electron effective mass in ZB ( $m_e^*/m_0 = 0.0795$ ) is smaller than the heavy hole mass of WZ ( $m_{HH}^{\parallel}/m_0 = 1.273$  and  $m_{HH}^{\perp}/m_0 = 0.158$ ). The same trend is also observed in the strained case. Also, since the bottom of the well in the conduction band has a higher value in the strained case, we can expect the interband transition energies to be blueshifted with the inclusion of strain effects.

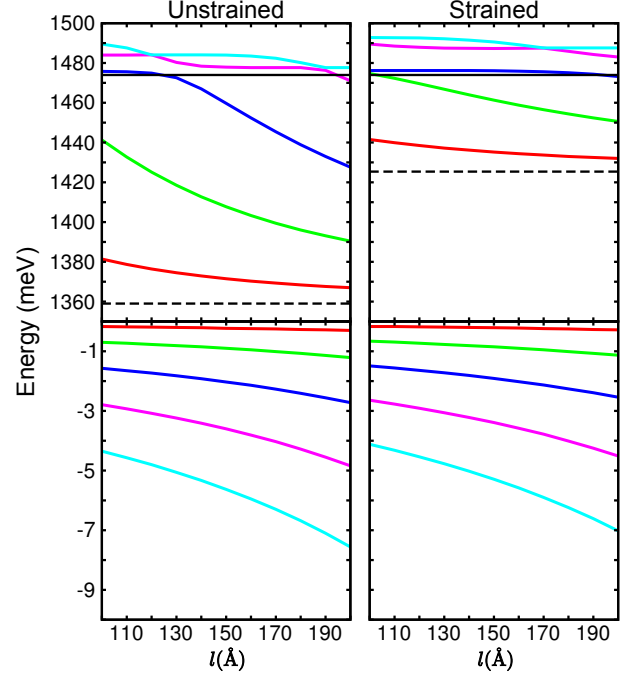


Figure 11. The first 5 states of the conduction and valence bands at  $\vec{k} = 0$  as a function of the ZB region width  $l$ . The solid line indicates the top of the conduction band well and the dashed line indicates the bottom.

The presence of strain effects gives rise to the piezoelectric polarization. For the InP ZB, the value for the piezoelectric constant used was  $e_{14} = 0.035 \text{ C/m}^2$ , taken from Ref. [44]. For both crystal structures, the value used for static dielectric constant was 12.5. The unknown parameter is the spontaneous polarization for WZ InP. Ref. [32] suggests that this value is smaller than that of InN ( $-0.03 \text{ C/m}^2$ ). In an attempt to estimate this value for InP, we performed the band structure calculations considering a range of values for  $P_{sp}$ .

The energy of the first 5 conduction and valence band states at  $\vec{k} = 0$  as a function of spontaneous polarization in WZ InP for three different ZB region widths is presented in Figure 12. The considered values for spontaneous polarization are  $-0.02 \text{ C/m}^2$ ,  $-0.015 \text{ C/m}^2$ ,  $-0.01 \text{ C/m}^2$ ,  $-0.005 \text{ C/m}^2$  and  $-0.001 \text{ C/m}^2$ . For  $l = 160 \text{ Å}$  and  $l = 200 \text{ Å}$  there is a crossing between the conduction and valence band states. This is not observed

experimentally therefore we consider this region *forbidden*. Then, the *allowed* values for spontaneous polarization considered here are then  $-0.01 \text{ C/m}^2$ ,  $-0.005 \text{ C/m}^2$  and  $-0.001 \text{ C/m}^2$ .

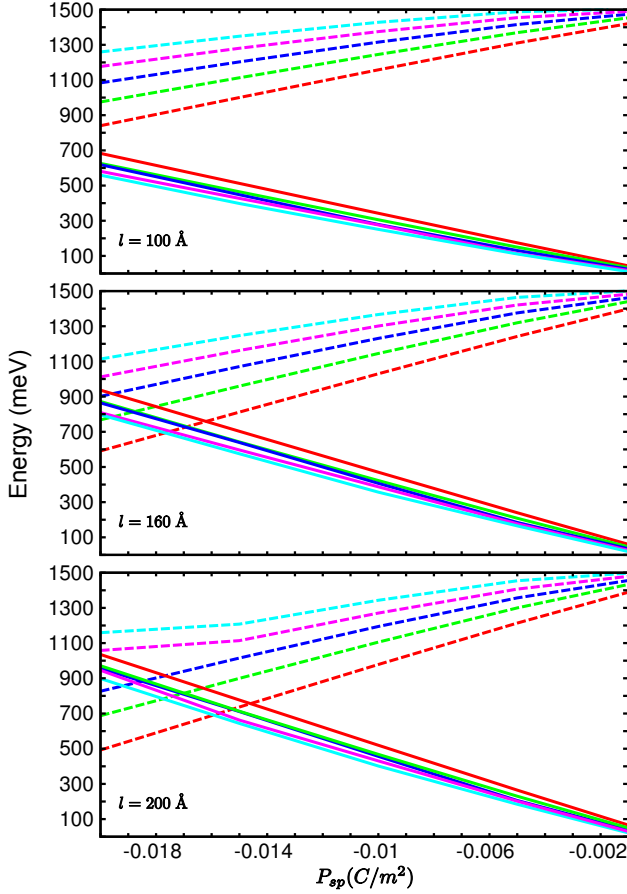


Figure 12. The first 5 states of the conduction and valence bands at  $\vec{k} = 0$  as a function of WZ spontaneous polarization  $P_{sp}$ . Notice the crossing of valence and conduction bands.

The diagonal potential profile including effects of piezoelectric and spontaneous polarization is presented in Figure 13. The ZB region is fixed at  $200 \text{ Å}$ . Analyzing these profiles, we expect to have strong coupling in the band structure for higher values of  $P_{sp}$  since the profiles are more close to each other. This induces the mixing of states because an energy value can be in more than one profile.

The resulting band structures for the three different potential profiles of Figure 13 are shown in Figure 14. For the three different values of  $P_{sp}$ , the conduction energy bands are nominated, from bottom to top, as EL1-EL9, composed of  $|c_{7,8}\rangle$  states. The valence bands, from top to bottom, are nominated as HH1-2, LH1, HH3, LH2, HH4-5, LH3, HH6, LH4, HH7, LH5, HH8, LH6, HH9, LH7, HH10, LH8, HH11, LH9, HH12, LH10, HH13, LH11, HH14, LH12, HH15, LH13, HH16,

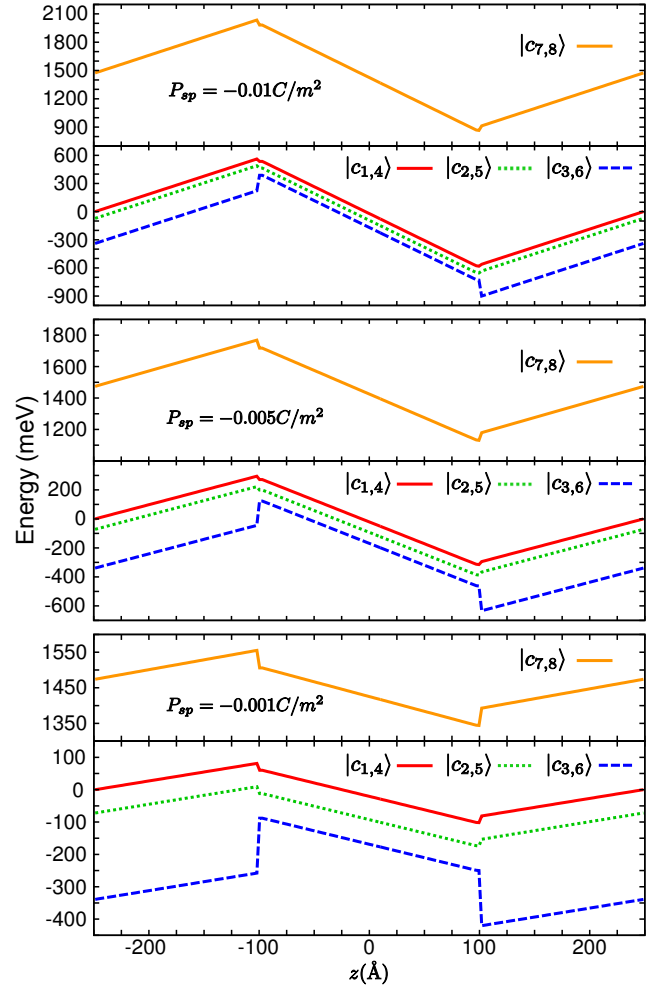


Figure 13. Diagonal potential profile of the Hamiltonian for the polytypical InP system considering strain, piezoelectric polarization in the ZB region and spontaneous polarization in the WZ region for  $l = 200 \text{ Å}$ . The values for the spontaneous polarization were chosen from Figure 12.

LH14, HH17, LH15 for  $P_{sp} = -0.01 \text{ C/m}^2$ ; HH1-3, LH1, HH4, LH2, HH5-6, LH3, HH7, LH4, HH8, LH5, HH9-10, LH6, HH11, LH7, HH12, LH8, HH13, LH9, HH14, LH10, HH15-16, LH11, HH17, LH12-13, HH18, LH14 for  $P_{sp} = -0.005 \text{ C/m}^2$  and HH1-7, LH1, HH8-9, LH2, HH10-11, LH3, HH12-13, LH4, HH14-15, LH5, HH16, LH6, HH17-18, LH7, HH19, LH8, HH20, LH9, HH21-22, LH10 for  $P_{sp} = -0.001 \text{ C/m}^2$ . The number of HH states increases as the value of  $P_{sp}$  decreases.

The anticrossings and also the spin splitting in the valence sub bands are more visible for higher values of  $P_{sp}$ . The strength of the resulting electric field not only increases the mixing of HH and LH states but also increases the value of the spin splitting in each sub band. This spin splitting is known as the Rashba effect [45] and is due to potential inversion asymmetry, even though the term  $\alpha(\vec{\sigma} \times \vec{k}) \cdot \vec{E}$  does not appear explicitly in the Hamiltonian

[46].

The number of confined states decreases as the spontaneous polarization decreases. On the other hand, the energy difference between the conduction and valence band ground state increases as the spontaneous polarization decreases, blueshifting the interband energy transitions.

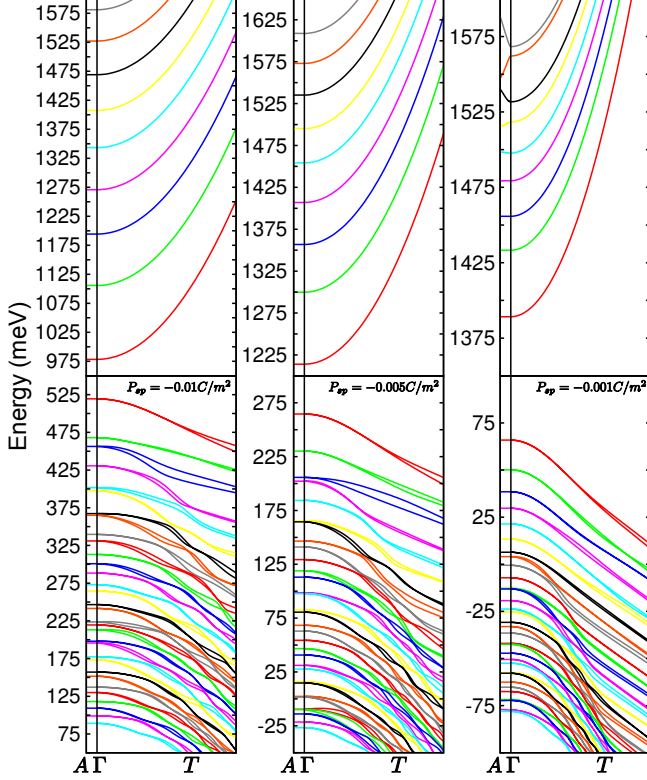


Figure 14. Band structure for the profiles presented in Figure 13. The spin-splitting of the energy bands is due to the field induced asymmetry.

The effect of piezoelectric and spontaneous polarization also induce carriers' spatial separation. This effect, in the probability densities in  $\vec{k} = 0$  can be seen in Fig. 15. The lowest four states of the conduction band and the highest four states of the valence band are presented. At  $\vec{k} = 0$  the wave functions of spin-up and spin-down are degenerated. We can see that the overlap increases for more excited states, also blueshifting the energy peak in the interband transitions. Since the potential profile is not completely even or odd, the envelope functions no longer have well defined parities.

## V. CONCLUSIONS

The basic result of this study is the theoretical model based on the k-p method and group theory concepts to calculate band structures of WZ/ZB polytypical systems in the vicinity of the band edge. The method allows us to

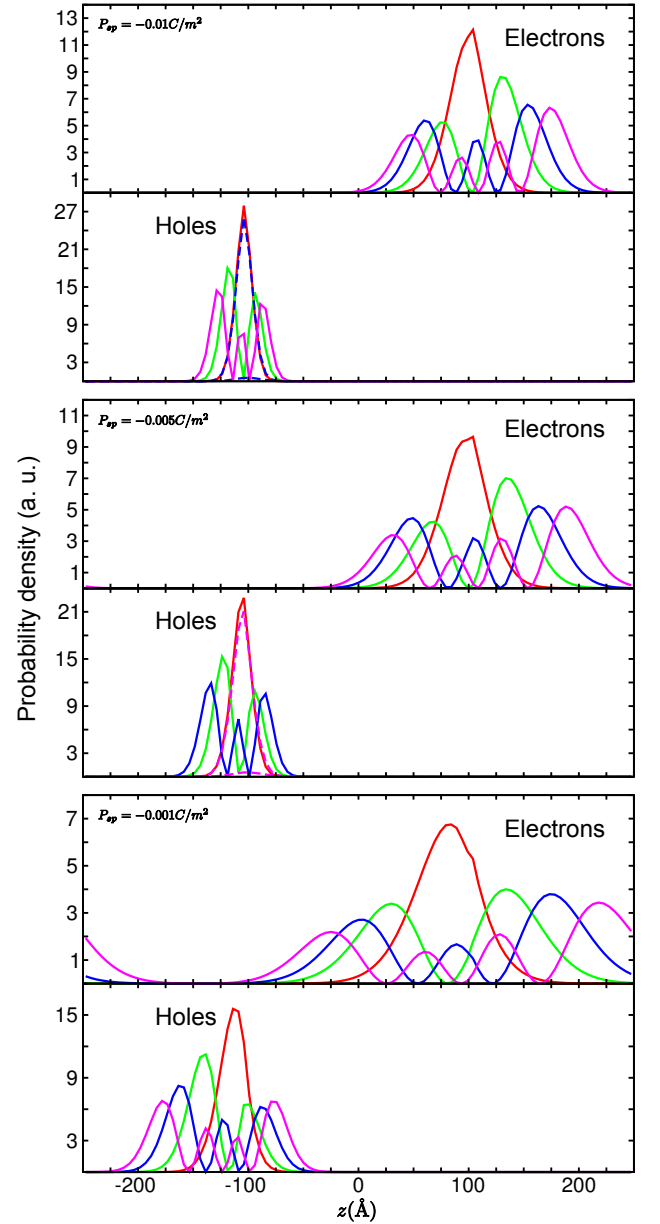


Figure 15. Probability densities at  $\vec{k} = 0$  for the lowest four states of the conduction band and the highest four states of the valence band of Fig. 14. The solid lines are the HH states and dashed lines represent the LH states.

describe in the same matrix Hamiltonian the ZB and WZ structures, with  $k_z$  along the [111] and [0001] directions, respectively. Since the WZ structure is less symmetric, the ZB parameters are assigned to the WZ ones. Our method not only is able to describe the k-p terms of the Hamiltonian but also includes the strain and polarization (spontaneous and piezoelectric) effects.

Extracting the parameters of WZ InP from Ref. [28] we applied our model to a WZ/ZB/WZ single well in order to understand the physics of the polytypical inter-

face. The potential profile at the interface WZ/ZB is type-II, whose feature is the spatial separation of carriers. The performed calculations in this study holds this characteristic.

Due to the lack of parameters in the literature for WZ InP, only the strain effect in the ZB region was considered here. This seems to be a reasonable consideration since the WZ structure is the dominant phase in NWs structures. However, such strain parameters would be fundamental in a system that the stable lattice constant is a intermediate value between WZ and ZB InP lattice parameters.

Within the limitation of strain, the piezoelectric polarization was also considered in the ZB region. For the WZ region, only the spontaneous polarization appears. Since there is no value in the literature for the spontaneous polarization of WZ InP, a range of values were considered in the simulations. Some of these values, however, induces a negative gap in the system. There is no data in the literature that corroborates this effect.

The proposed model, jointly with the obtained results, proved to be useful in the study of electronic band structures of WZ/ZB polytypical systems, such as NWs. Exploring the opportunities of band gap engineering considering not only different compounds, but also different crystal structures, could lead to the development of novel nanodevices.

## ACKNOWLEDGEMENTS

The authors acknowledge financial support from the Brazilian funding agencies CAPES and CNPq.

- 
- [1] Y. Cui, Q. Wei, H. Park, and C. M. Lieber, *Science* **293**, 1289 (2001)
  - [2] F. Patolsky, G. Zheng, and L. C. M., *Nanomedicine* **1**, 51 (2006)
  - [3] G. Zheng, F. Patolsky, Y. Cui, W. U. Wang, and C. M. Lieber, *Nature Biotechnology* **23**, 1294 (2005)
  - [4] X. Duan, Y. Huang, R. Agarwal, and C. M. Lieber, *Nature* **421**, 241 (2003)
  - [5] X. Duan, Y. Huang, Y. Cui, J. Wang, and C. M. Lieber, *Nature* **409**, 66 (2003)
  - [6] H. Ng, J. Han, T. Yamada, and P. Nguyen, *Nano Letters* **4**, 1247 (2004)
  - [7] R. S. Wagner and W. C. Ellis, *Applied Physics Letters* **4**, 89 (1964)
  - [8] V. Dubrovskii, G. Cirlin, and V. Ustinov, *Semiconductors* **43**, 1539 (2009)
  - [9] Y. Kitauchi, Y. Kobayashi, K. Tomioka, S. Hara, K. Hiruma, T. Fukui, and J. Motohisa, *Nano Letters* **10**, 1699 (2010)
  - [10] J. Johansson, L. S. Karlsson, C. P. T. Svensson, T. Mårtensson, B. A. Wacaser, K. Deppert, L. Samuelson, and W. Seifert, *Nature Materials* **5**, 574 (2005)
  - [11] P. Caroff, K. A. Dick, J. Johansson, M. E. Messing, K. Deppert, and L. Samuelson, *Nature Nanotechnology* **4**, 50 (2009)
  - [12] S.-G. Ihn, J.-I. Song, Y.-H. Kim, J. Y. Lee, and I.-H. Ahn, *IEEE Transactions on Nanotechnology* **6**, 384 (2007)
  - [13] J. Bao, D. C. Bell, F. Capasso, N. Erdman, D. Wei, L. Fröberg, T. Mårtensson, and L. Samuelson, *Advanced Materials* **21**, 3654 (2009)
  - [14] J. Bolinsson, P. Caroff, B. Mandl, and K. A. Dick, *Nanotechnology* **22**, 265606 (2011)
  - [15] C. Thelander, P. Caroff, S. Plissard, A. W. Dey, and K. A. Dick, *Nano Letters* **11**, 2424 (2011)
  - [16] K. A. Dick, P. Caroff, J. Bolinsson, M. E. Messing, J. Johansson, K. Deppert, L. R. Wallenberg, and L. Samuelson, *Semiconductor Science and Technology* **25**, 024009 (2010)
  - [17] G. Dresselhaus, *Physical Review* **100**, 580 (1955)
  - [18] E. O. Kane, *Physics of III-V compounds*, Semiconductors and Semimetals, Vol. 1 (Academic Press, New York, 1966)
  - [19] G. E. Pikus, *Soviet Physics JETP* **14**, 898 (1962)
  - [20] G. Bir and G. Pikus, *Symmetry and strain-induced effects in semiconductors* (Wiley, New York, 1974)
  - [21] S. L. Chuang and C. S. Chang, *Physical Review B* **54**, 2491 (1996)
  - [22] G. Bastard and J. A. Brum, *IEEE Journal of Quantum Electronics* **22**, 1625 (1986)
  - [23] G. M. Sipahi, R. Enderlein, L. M. R. Scolfaro, and J. R. Leite, *Physical Review B* **53**, 9930 (1996)
  - [24] S. C. P. Rodrigues, G. M. Sipahi, L. M. R. Scolfaro, and J. R. Leite, *Applied Physics Letters* **76**, 1015 (2000)
  - [25] L. C. Chuang and C. S. Chang, *Semiconductor Science and Technology* **12**, 252 (1997)
  - [26] S. C. P. Rodrigues and G. M. Sipahi, *Journal of Crystal Growth* **246**, 347 (2002)
  - [27] M. Murayama and T. Nakayama, *Physical Review B* **49**, 4710 (1994)
  - [28] A. De and C. E. Pryor, *Physical Review B* **81**, 155210 (2010)
  - [29] K. Pemasiri, M. Montazeri, R. Gass, L. M. Smith, H. E. Jackson, J. Yarrison-Rice, S. Paiman, Q. Gao, H. H. Tan, C. Jagadish, X. Zhang, and J. Zou, *Nano Letters* **9**, 648 (2009)
  - [30] S. Paiman, Q. Gao, H. H. Tan, C. Jagadish, K. Pemasiri, M. Montazeri, H. E. Jackson, L. M. Smith, J. M. Yarrison-Rice, X. Zhang, and J. Zou, *Nanotechnology* **20**, 225606 (2009)
  - [31] E. G. Gadret, G. O. Dias, L. C. O. Dacal, M. M. de Lima Jr., C. V. R. S. Ruffo, F. Iikawa, M. J. S. P. Brasil, T. Chiaramonte, M. A. Cotta, L. H. G. Tizei, D. Ugarte, and A. Cantarero, *Physical Review B* **82**, 125327 (2010)
  - [32] L. Zhang, J.-W. Luo, A. Zunger, N. Akopian, V. Zwiller, and J.-C. Harmand, *Nanoletters* **10**, 4055 (2010)
  - [33] D. Li, Z. Wang, and F. Gao, *Nanotechnology* **21**, 505709 (2010)
  - [34] L. C. O. Dacal and A. Cantarero, *Solid State Communications* **151**, 781 (2011)
  - [35] M. Moewe, L. C. Chuang, V. G. Dubrovskii, and C. Chang-Hasnain, *Journal of Applied Physics* **104**, 044313 (2008)
  - [36] M. S. Dresselhaus, G. Dresselhaus, and A. Jorio, *Group Theory: application to the physics of condensed matter* (Springer-Verlag, 2008)

- [37] P. E. Faria Junior and G. M. Sipahi, <http://arxiv.org/abs/1012.0227>(2010)
- [38] S. H. Park and S. L. Chuang, *Journal of Applied Physics* **87**, 353 (2000)
- [39] I. Vurgaftman, J. R. Meyer, and L. R. Ram-Mohan, *Journal of Applied Physics* **89**, 5815 (2001)
- [40] S. L. Chuang and C. S. Chang, *Applied Physics Letters* **68**, 1657 (1996)
- [41] C. Mailhot and D. L. Smith, *Physical Review B* **35**, 1242 (1987)
- [42] P. Harrison, *Quantum Wells, Wires and Dots: Theoretical and Computational Physics of Semiconductor Nanostructures* (John Wiley and Sons Ltd, 2006)
- [43] G. Bastard, *Wave mechanics applied to semiconductor heterostructures* (Halsted Press, Les Ulis Cedex, France, 1988)
- [44] H. Magnus, M. E. Pistol, and C. Pryor, *Journal of Applied Physics* **92**, 932 (2002)
- [45] Y. A. Bychkov and E. I. Rashba, *Journal of Physics C: Solid State Physics* **17**, 6039 (1984)
- [46] R. Winkler, *Spin-orbit coupling effects in two-dimensional electron and hole systems* (Springer, Berlin, 2003)